IEEE Access
Multidisciplinary | Rapid Review | Open Access Journal

Received 21 October 2023, accepted 19 November 2023, date of publication 28 November 2023,
date of current version 6 December 2023.

Digital Object Identifier 10.1109/ACCESS.2023.3337524

RESEARCH ARTICLE

A Lean Approach to Zero and Low-Speed Sensorless Control of PMaSynRMs

A. TAP[1,2], K. AKGUL[2], A. F. ERGENC[3], M. YILMAZ[2], (Senior Member, IEEE), AND L. T. ERGENE[2], (Senior Member, IEEE)

[1]E-Drive Systems and Controls, AVL Research and Engineering Turkey, 34885 Istanbul, Turkey
[2]Department of Electrical Engineering, Istanbul Technical University, 34469 Istanbul, Turkey
[3]Department of Control and Automation Engineering, Istanbul Technical University, 34469 Istanbul, Turkey

Corresponding author: A. Tap (alper.tap@avl.com)

This work was supported in part by The Scientific and Technological Research Council of Turkey (TÜBİTAK) under Grant 120E375, and in part by Istanbul Technical University Scientific Research Projects Coordination Unit (ITU-BAP) under Grant 43149.

ABSTRACT Sensorless control of permanent magnet motors in full speed range is indispensable for home appliance applications due to cost, robustness and maintenance requirements. Zero and very low-speed sensorless control is a challenging area for model-based position observers. The common methodology for position detection at zero and low speeds is high-frequency signal injection methods due to their independence from model parameters. The major drawback of such methods is the signal processing burden for demodulation of resultant high-frequency currents. In this study, a simplified filtering scheme with a reduced number of filters is proposed for high-performance zero and low speed control of the Permanent Magnet Assisted Synchronous Motors for washing machine applications with a low-cost microcontroller. The proposed method employs the rotating voltage vector injection using a single band-pass filter combined with N-sample averaging. This approach reduces system complexity by reducing the number of filtering stages to just one while providing robustness to estimations under fast current and speed gradients. The proposed method leaves 47% CPU overhead (without any optimization) including notch filtering of the dq-axes current feedbacks for better current control and parallel operation with an SMO based Back-EMF observer for switchover at higher speeds. Experimental results show that the proposed method is suitable for a low-cost microcontroller implementation in a washing machine with maximum uncompensated and compensated errors of 2.28 and 0.708 degree electrical respectively. The position estimation algorithm is shown to be suitable for unfavorable operating conditions such as zero speed acceleration under full load, step speed commands, step direction reversals, intermittent loads such as changing drum inertia and pulsating torque at very low speeds. The proposed system is able to track position with position errors up to 0.708 degree electrical and maintain speed control at very low speeds under 30% pulsating load torque.

INDEX TERMS High-frequency voltage injection, permanent magnet assisted synchronous reluctance motor, sensorless control, extended EMF.

NOMENCLATURE

u_α, u_β	α- and β-axis voltage.
u_d, u_q	d- and q-axis voltage.
i_s	Stator current vector magnitude.
i_α, i_β	α- and β-axis current.
i_d, i_q	d- and q-axis current on rotor reference frame.
i^{hf}	High/low frequency component current.
u^{hf}	High/low frequency component voltage.
V_{hf}	High-frequency voltage amplitude.
R_s	Stator winding resistance.
L_d, L_q	d- and q-axis inductance.
λ_{PM}	Permanent magnet flux.
ω_e	Electrical frequency.
ω_h	High-frequency angular speed.
T_e	Electromagnetic torque.
θ_e	Electrical rotor position.
$\theta_{e,est}$	Estimated electrical rotor position.
f_g	Bandwidth frequency of band-pass filter.
f_0	Center frequency of band-pass filter.
θ_{q+}, θ_{q-}	Estimated $\pm$q-axis angle.

The associate editor coordinating the review of this manuscript and approving it for publication was Jinquan Xu.

I. INTRODUCTION

The home appliance market is one of the most competitive markets in today's industry. Many companies deliver white goods with electric motors such as washers, dryers, refrigerators, vacuums and small kitchen appliances, both low-end and high-end products. Most of the time, in a medium to high end product, when an electric motor is present, it is either a permanent magnet synchronous motor (PMSM) or a permanent magnet assisted synchronous reluctance motor (PMaSynRM), due to their comparable power density, efficiency, cost (ferrites), ease of control and lower maintenance requirements. Another option is to use induction motors, but they are being replaced by permanent magnet motors due to more stringent efficiency requirements in the appliance market [1].

Most of the time, these types of motors are coupled with an electric drive unit, which is an inverter hardware alongside a control software. Rotor position information is obtained either with a position sensor or with sensorless methods. Whenever possible, employing sensorless Field Oriented Control (FOC) methods is always beneficial in terms of cost and robustness, as well as less maintenance requirements.

The sensorless control methods are divided into two categories; zero to low-speeds and medium to high-speeds [2]. These two categories have different needs for rotor position observer design. For the zero to low-speed region, since the exciting features of the measured fundamental electrical variables are low due to the low speed, combined with the measurement noise, model-based observers do not perform very well. For this speed region, additional identifying signal injection is often required. This signal injection is in the form of superimposed voltages or currents [3]. With proper demodulation of the measured signals, the rotor position is obtained, provided that the response to the injected signals is sufficient in the sense of amplitude and Signal-to-Noise-Ratio (SNR). Other methods such as the third harmonic observers, zero crossing detection algorithms, current rate of change (switching transient) algorithms [4], zero sequence voltage observers [2], some of which being parameter dependent and some parameter free, are also available for low speed operating ranges. Because of aforementioned reasons, back-EMF and signal injection based methods are commonly combined to account for sensorless FOC in the whole speed range [5], [6]. On the other hand, in the medium to high-speed range, model-based rotor position observers perform well as there is a good signal-to-noise ratio of the back-EMF and measured variables are high enough for convergence of the observed rotor position. The main drawback of these methods is sensitivity to parameter variations or parameter uncertainties. Parameter independency is also another important aspect of the position estimation methods as parameters might be uncertain at extreme operating points for highly nonlinear machines like synchronous reluctance machines (SynRMs) or machines with higher slotting effects and concentrated windings.

Injected signals are either voltages or currents hence the names high-frequency voltage injection (HFVI) and high-frequency current injection (HFCI). HFVI is straightforward in the sense that no additional hardware or software modification to a conventional FOC scheme is required. In the HFVI, HF components of suitable magnitude and frequency are superimposed on the voltage reference of the inverter. The system current response to these superimposed components is then analyzed and position information contained within them is extracted since the current response of the magnetically salient machines is modulated with the rotor position. HFVI is also advantageous in terms of low torque ripples. If the amplitude is not enough to provide a good estimate, HF voltage magnitude can always be regulated to provide a converging estimate, a feature not so easy to implement in the HFCI methods [7]. In the HFCI method, HF current components superimposed to the current set points are regulated with the current controllers. This is often problematic in terms of bandwidth with the conventional FOC current regulators, therefore some adjustments, including sensor replacement, to the controllers might be necessary [3].

Among the voltage injection methods, the most popular two are the sinusoidal rotating HFVI (HFRVI) and pulsating HFVI (HFPVI) method. HFRVI is usually applied to sensorless control of PMSM with large saliencies like PMaSynRM. The pulsating HFI is used for PMSMs with smaller saliencies. Comparing these two methods, pulsating voltage injection methods have the advantage of a simpler filtering structure but suffer from dynamic performance issues. On the other hand, rotating signal injection is robust to environmental factors such as noise and system nonlinearities, but has more complicated filtering schemes with good dynamic performance.

In the HFPVI method, the injection is carried out in the estimated d-q rotating reference frame. Although the injected voltage signal is sinusoidal, it is pulsating in the stationary reference frame. A pulsating voltage vector of a significantly higher frequency than the fundamental frequency is superimposed on the estimated axis of choice, either d or q [5]. With driving the complex part in the current response to zero with the use of a regulator, the actual rotor position can be estimated. This method is also susceptible to multiple saliencies. Both voltages or currents can be injected considering either the stationary frame or the estimated frame [2], [6]. The HF signals are generally superimposed with two-phase stationary voltages and they are sinusoidal with constant amplitudes. The decomposed HF currents from the motor phase currents contain the rotor position information and it can be obtained with various signal processing techniques [8].

The injection in the stationary reference frame becomes more advantageous because the knowledge of the position

information is needed for injection in the rotating reference frame. In the injection methods carried out in the d-q axes, the estimated rotating reference frame is used according to the estimated position and these methods are directly related to the estimation success. The peak-to-peak error of estimated position increases with motor speed [10]. In addition, both the estimated position and speed ripples increase with increasing load as well as during speed transients [11], [12]. Peak-to-peak estimation error also dramatically increases at higher speeds in [13] where HFRVI is used. Fluctuations in both speed and position at low speeds are attributed to the high inertia of the shaft. In the case of HFRVI technique, the position estimation error and ripple increase with the shaft load [14], [15]. Nevertheless, the ripple is almost the same at zero motor speed for stall torque situation.

Anisotropic nature of PMaSynRM creates strong saliencies. Saliencies may be affected by saturating factors such as magnet flux amount and loading. HF injection methods track spatial saliencies. These saliencies are created either by distinct rotor and stator structures or by saturated regions. Saliencies can be sinusoidal with harmonics or non-uniform. For sinusoidal saliencies, current or voltage response will be modulated sinusoidally and requires proper demodulation and position extraction. HFI methods are affected from all types of saliencies including single and harmonic saliencies, rotor slotting, magnetic anisotropy, magnet flux, loading, saturation and cross saturation [9], [16]. The complete erroneous detection of d-axis is also possible. Inverter switching distortions and analog/digital filtering of the carrier signals should also be evaluated [12], [17], [18].

Due to their highly salient structure of the SynRMs, PMaSynRMs and PMSMs, voltage injection methods perform very well [9]. As the d-axis inductance is much higher than the q-axis inductance, HF response during rotor rotation is varied considerably, leading to easier demodulation and position determination of such motors. To account for offsets and position independent errors, compensation methods are proposed which are created via off-line tests [9]. Another major advantage for the PMaSynRMs is that the HF methods are nearly insensitive to parameter variations, as there is already a better spatial separation of the saliency. This feature makes it a suitable method for PMaSynRMs as they suffer from heavy saturation under full and overload cases.

A few problems are associated with the HF injection in PMaSynRMs like the selection for correct injected voltage amplitude and frequency, the magnet polarity detection, filter computing burden and total processing delay caused by filtering. In order to determine the injected frequency, a clear spectral analysis is required.

Detection of the modulating effect of the rotor saliency for position determination is not enough in the case of a highly salient PM motor. Magnet polarity also needs to be determined for correct field orientation. The most popular algorithm for magnet polarity detection is the stationary current response for PMSMs. This method has some drawbacks especially for PMaSynRMs, which have much lower magnet flux compared to PMSMs. The magnitude of the voltage is another concern as the HF currents may cause acoustic noises. The HF voltage amplitude should be chosen larger in the time of speed transients to increase estimation performance during transients and reduce acoustic noise for the steady state condition [9], [19], [20].

Efforts for simplifying the conventional HFI methods are present in the current literature. For the pulsating voltage injection for position determination of SynRMs, two studies omit the band-pass filtering and reduce the whole system to two low-pass filters, but the operation requires an injected voltage magnitude as high as 37% of the DC bus [21]. Another study proposes a similar method for surface-mounted PMSMs, which pose difficulty due to a lack of prominent saliency [22]. A simplified HFI method consisting of only one LPF is proposed, but only for initial position detection of the rotor and not for closed-loop position feedback [23]. In a completely filterless solution including current feedback, injecting a specific voltage vector in between normal switching cycles to determine position is proposed [24]. However, the method suffers from inverter nonlinearities that cause the misalignment of the intended voltage vector.

Current simplified methods in the literature are revolving around pulsating voltage injection. In this paper, a simplification to a rotating voltage vector injection is carried out, which has the aforementioned advantages over the pulsating voltage injection. Combined with the highly salient nature of the PMaSynRM and proposed approach, a simple and robust system compared to the conventional method is synthesized. Proposed method provides the following advantages compared to the conventional HFVI:

- Providing high accuracy up to 0.708 degrees electrical at low-speed region.
- Reduction in total filtering steps for signal processing from two to one.
- Reduction in total coordinate transformations by half.
- Estimation with very low (down to 5% of DC link) and constant injected rms voltage value for both transients and steady state.
- Band-stop/notch filtering of the phase currents for smooth current feedback with less delay and better current control.
- Using full bandwidth of current controllers for faster current response during FOC due to a decreased disruption of current feedback.
- Better control over delay compensation because of reduced number of filters
- Simple structure and less design effort and simple implementation on low-cost microcontroller units (MCU) suited for home appliances

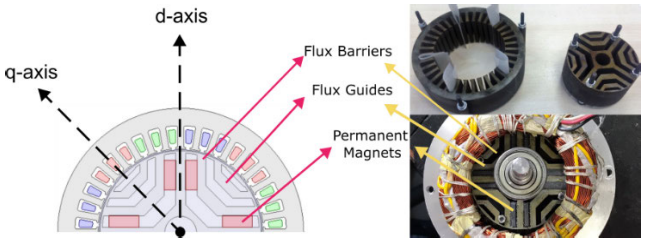

FIGURE 1. Cross sectional view of PMaSynRM with the motor in this study (before assembly).

II. MATHEMATICAL MODEL AND HFI SENSORLESS CONTROL OF PMaSynRM

PMaSynRMs generate torque using magnetic reluctance and permanent magnet flux. Compared to an IPMSM, the contribution of reluctance torque is much greater in the overall torque. This is possible with distinct geometries that optimize the generated reluctance torque, such as using highly salient magnetic structures with flux barriers and flux guides – a geometry designed to create strong anisotropy. Fig. 1 shows the cross section of the PMaSynRM with its d-q axes and the motor used in this study with parameters given in Table 1. Anisotropy property makes SynRMs & PMaSynRMs good candidates for HFI methods as there is a significant difference in the high-frequency current response depending on the rotor position since the d & q axes inductances are considerably different.

Fundamental voltage equations of the PMaSynRMs neglecting the saturation, cross saturation, and iron loss in the d-q frame are given in (1). This model is the basis for the HF model and extended-EMF (EEMF) model of the PMaSynRM.

$$\begin{bmatrix} u_d \\ u_q \end{bmatrix} = \begin{bmatrix} R_s + pL_d & -\omega_e L_q \\ \omega_e L_d & R_s + pL_q \end{bmatrix} \begin{bmatrix} i_d \\ i_q \end{bmatrix} + \begin{bmatrix} \omega_e \lambda_{PM} \\ 0 \end{bmatrix} \quad (1)$$

The resultant d&q-axis equivalent circuits are given in Fig. 2. Torque equation of the PMaSynRM in the d-q frame is given in (2).

$$T_e = \frac{3}{2} p \left[\lambda_{PM} i_d + \left(L_d - L_q \right) i_d i_q \right] \quad (2)$$

Throughout the paper, in all control schemes, current references are calculated using the Maximum Torque per Ampere (MTPA) rule derived from (2). MTPA is also regarded as a maximum efficiency trajectory for very low-speed and medium-speed operations where the copper losses are dominant in the lower end of the speed interval.

The motor used in this study is a three-phase four pole PMaSynRM with 375 W of rated power. This is a motor designed to be used in a washing machine consisting of 36 stator slots, incorporating a full pitched distributed winding with a stator outer diameter of 118 mm. The rotor has three flux barriers per pole and magnets are placed at the end of flux barriers as given in Fig. 1.

The MTPA rule for PMaSynRM is given for the q-axis current in (4), while the d-axis current is then inferred using (3) for the PMaSynRM.

TABLE 1. Parameters of the PMaSynRM.

Parameter	Value
Rated Power	375 [W]
Rated Torque	1.2 [Nm]
Number of Pole Pairs	2
Number of Slots	36
Stator Outer Diamater	118 mm
Stack Length	32 mm
Rated Phase Current	1.62 [A]
Base Frequency	100 Hz
Stator Phase Resistance	5.9 [Ω]
d-axis Inductance	182 [mH]
q-axis Inductance	67 [mH]
Permanent Magnet Flux	96 [mWb]

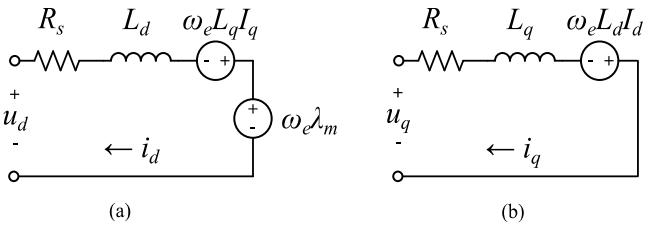

FIGURE 2. D- and q-axis equivalent circuits of a PMaSynRM.

$$i_s = \sqrt{i_d^2 + i_q^2} \quad (3)$$

$$i_{qMTPA} = \frac{-\lambda_{PM} + \sqrt{\lambda_{PM}^2 + 8 i_s^2 \left(L_d - L_q \right)^2}}{4 \left(L_d - L_q \right)} \quad (4)$$

Resulting MTPA trajectory for the motor defined in Table 1 in combination with (3) and (4) is given in Fig. 3 alongside the current limit circle and voltage limit ellipse at base speed. The current limit circle and voltage limit ellipse intersection area defines the possible operating points. To adjust to low-cost MCUs and save computation time, the MTPA rule is implemented as a look-up table instead of a real-time calculation during the testing process.

A. HF MODEL OF THE PMaSynRM

In order to deal with the high-frequency currents resulting from the high-frequency voltage injection, a high-frequency model of the PMaSynRM is needed. The mathematical model of PMaSynRM in the rotating reference frame given in (1) is transformed to the stationary reference frame.

Considering the high-frequency nature of the injected voltages and low-speed operating region, the resistance and motor speed-dependent terms may be omitted, leaving only the high-frequency inductances [13], [14].

As a result, the model in (1) takes the form of (5) in the $\alpha\&\beta$ reference frame.

$$u_{\alpha\beta}^{hf} = L\left(\theta_e\right) \frac{d}{dt} \left(i_{\alpha\beta}^{hf} \right) \quad (5)$$

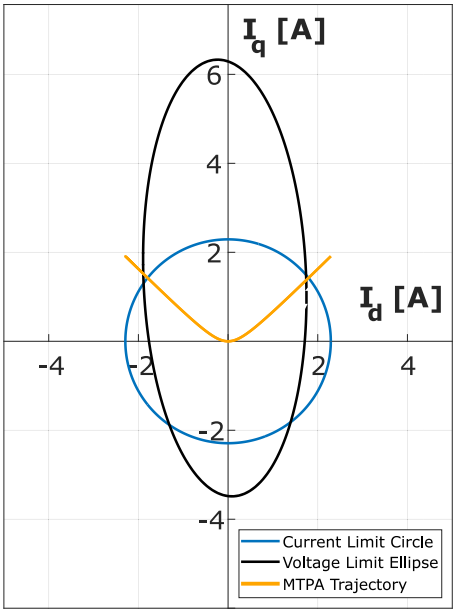

FIGURE 3. MTPA trajectory for the PMaSynRM defined in Table 1.

The high-frequency inductance matrix $L(\theta_e)$ and its components are given in (6) and (7).

$$L(\theta_e) = \begin{bmatrix} L_0 + L_1 cos(2\theta_e) & L_1 \sin(2\theta_e) \\ L_1 \sin(2\theta_e) & L_0 - L_1 cos(2\theta_e) \end{bmatrix} \quad (6)$$

where;

$$L_0 = \frac{L_d + L_q}{2}; L_1 = \frac{L_d - L_q}{2} \quad (7)$$

The differential model in the stationary reference frame, (8) is obtained when (5) is rearranged with (6) and (7).

$$\frac{d}{dt}\begin{bmatrix} i_\alpha^{hf} \\ i_\beta^{hf} \end{bmatrix} = \frac{1}{L_d L_q}\begin{bmatrix} L_0 - L_1 cos(2\theta_e) & -L_1 \sin(2\theta_e) \\ -L_1 \sin(2\theta_e) & L_0 + L_1 cos(2\theta_e) \end{bmatrix}\begin{bmatrix} u_\alpha^{hf} \\ u_\beta^{hf} \end{bmatrix} \quad (8)$$

B. HF VOLTAGE INJECTION

A voltage component with a certain amplitude and frequency is superimposed over the current controller outputs to generate high-frequency currents that are modulated with double of the rotor electrical position. The selected amplitude and frequency of the injected voltage are of crucial value as they determine the amplitude of the high-frequency current generated. The amplitude and frequency of the injected voltage should be as high as possible to generate high-frequency currents that have high SNRs. At the same time, they should have as low magnitude as possible so that the HF currents don't cause high losses, induce high torque ripple, and generate acoustic noise. This poses a trade-off, and optimal solution often depends on the machine at hand. The HF voltages $u_{\alpha\beta}^{hf}$ to be injected are given in (9) [25].

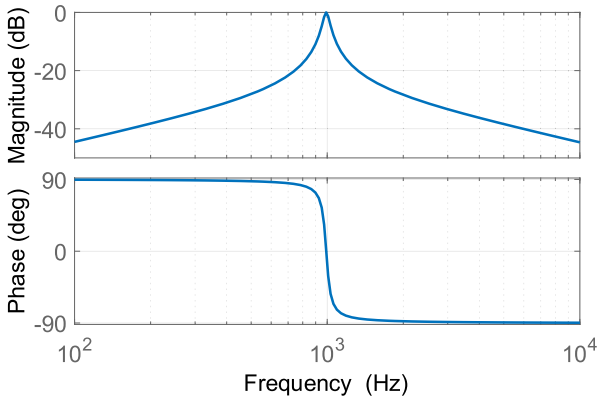

FIGURE 4. Bode plot of the band-pass filter.

$$u_{\alpha\beta}^{hf} = \begin{bmatrix} u_\alpha^{hf} \\ u_\beta^{hf} \end{bmatrix} = V_{hf}\begin{bmatrix} -sin(\omega_h t) \\ cos(\omega_h t) \end{bmatrix} \quad (9)$$

When this voltage is applied, HF stator currents $i_{\alpha\beta}^{hf}$ are obtained as in (10). These currents contain the position information in the negative sequence component.

$$i_{\alpha\beta}^{hf} = \begin{bmatrix} i_\alpha^{hf} \\ i_\beta^{hf} \end{bmatrix} = \begin{bmatrix} I_{i0} cos(\omega_h t) - I_{i1} cos(2\theta_e - \omega_h t) \\ I_{i0} sin(\omega_h t) - I_{i1} sin(2\theta_e - \omega_h t) \end{bmatrix} \quad (10)$$

The positive sequence component I_{i0} and the negative sequence component I_{i1} are given in (11).

$$I_{i0} = \frac{V_{hf} L_0}{\omega_h L_d L_q}; I_{i1} = \frac{V_{hf} L_1}{\omega_h L_d L_q} \quad (11)$$

HF currents are first isolated and then subjected to several processes to obtain the position information in the negative sequence component $-I_{i1}$ [14].

The block diagram of the entire system is given in Fig. 5. Firstly, three-phase currents are transformed to a two-phase stationary frame with Clarke transformation. After that, Park transformation ($\alpha\beta 0$-$dq0$) to a positive high-frequency frame is applied to the currents with the angle ($\omega_h t$) in order to band-pass filter the negative sequence component. The resulting currents in the positive high-frequency frame are given in (12) where I_s is the torque producing fundamental stator current's magnitude.

$$i_{dq}^{hf+} = \begin{bmatrix} i_d^{HF+} \\ i_q^{HF+} \end{bmatrix} = \begin{bmatrix} I_s cos(\omega_e t - \omega_h t) \\ I_s sin(\omega_e t - \omega_h t) \end{bmatrix} + \begin{bmatrix} I_{i0} - I_{i1} cos(2\theta_e - 2\omega_h t) \\ I_{i0} - I_{i1} sin(2\theta_e - 2\omega_h t) \end{bmatrix} \quad (12)$$

Constant value I_{i0} and torque producing fundamental current are then filtered utilizing a band-pass filter at the negative sequence frequency. The important thing to note here is that the fundamental torque producing the stator current component will not have enough spectral separation from the negative rotating component when transformed to the positive

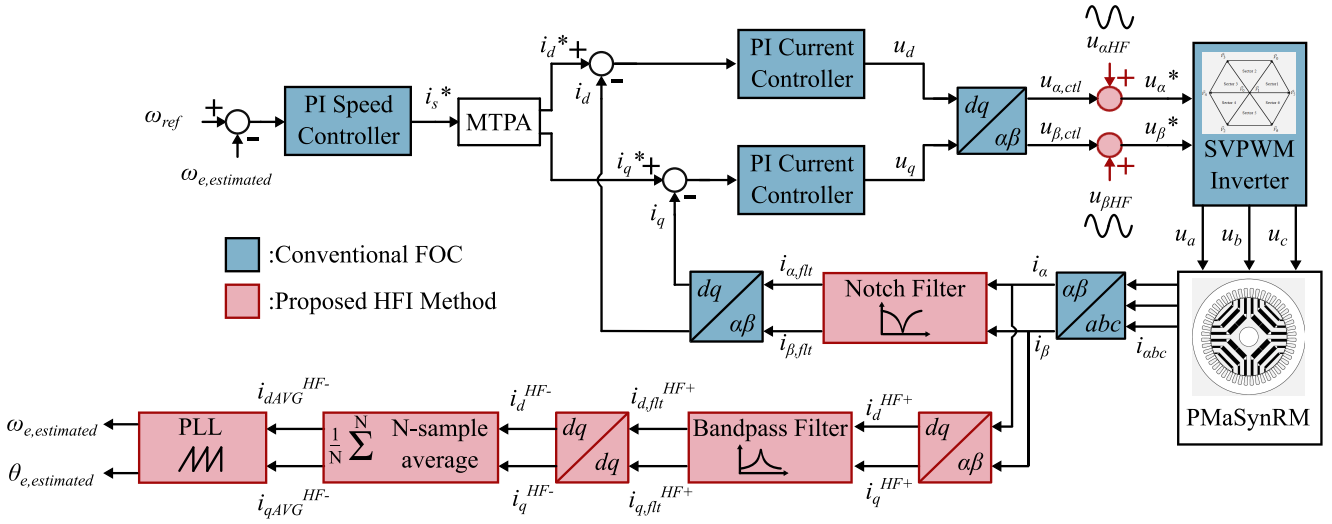

FIGURE 5. Block diagram of the entire system.

high-frequency frame. Instead of using a combination of high-pass at positive frame and low pass at negative frame to remove the I_s and I_{i0} components, the whole spectrum is band-pass filtered for the negative frequency component. This reduces the number of transformations required and simplifies the system. For simpler implementation, the band-pass filter order is kept at a minimum, resulting in a shallow roll-off at the magnitude response.

Since I_s magnitude is very large at full load compared to the high-frequency components and band-pass filter roll-off is not too steep, torque producing stator current will leak into the spectrum of the filter output but with a small gain at a frequency $(\omega_e - \omega_h)$. This leakage causes ripple in the modulated negative frequency components and will distort estimation. Mitigation of this spectral leakage is achieved using an N-sample averaging filter.

The transfer function of the band-pass filter is given in (13) where f_g is the bandwidth frequency, and f_0 is the center frequency.

$$G_{BPF}(s) = \frac{2\pi f_g s}{s^2 + 2\pi f_g s + (2\pi f_0)^2} \tag{13}$$

The center frequency is adjusted so that at both zero and switchover frequency, near unity gain and zero phase to the negative sequence components are obtained. Otherwise, the pass-band and center frequency can be adjusted so that the effects of the stator fundamental current are minimized. Fig. 4 gives the Bode plot of the band-pass filter. For this study, the center frequency is chosen as 1000 Hz with a pass-band of 164 Hz. This is a good trade-off for minimizing the 500-510 Hz band for the leakage, unity gain and phase for negative sequence components. Resulting discretized filter has -7 degree phase shift and near unity gain for the negative sequence component while it allows nearly 4% of the stator fundamental current to pass through.

The output of the band-pass filter in positive high-frequency frame is given in (14). These currents are then transformed to the negatively rotating HF frame, resulting in dq-axes currents as a function of double the electrical rotor position as in (15).

$$i_{dq}^{HF+} = \begin{bmatrix} i_d^{HF+} \\ i_q^{HF+} \end{bmatrix} = \begin{bmatrix} -I_{i1} cos\,(2\theta_e - 2\omega_h t) \\ -I_{i1} sin\,(2\theta_e - 2\omega_h t) \end{bmatrix} \tag{14}$$

$$i_{dq}^{HF-} = \begin{bmatrix} i_d^{HF-} \\ i_q^{HF-} \end{bmatrix} = \begin{bmatrix} -I_{i1} cos\,(2\theta_e) \\ -I_{i1} sin\,(2\theta_e) \end{bmatrix} \tag{15}$$

Lastly, since only a single band-pass filter is used, one should expect a very narrow pass-band and high roll-off on the filter, which corresponds to a region that should include the negative rotating component of the high-frequency currents. When a narrow pass band filter is designed without increasing the filter order, phase and gain response deteriorates from the desired values and the roll-off is limited. Considering (12) under a steady state condition, the positive rotating component is DC at the positive rotating reference frame. This does not cause an issue for the band-pass filter.

On the other hand, the fundamental component of the torque producing current at $(\omega_e$-$\omega_h)$ does not have good spectral separation from the negative rotating component, considering the pass-band and steep roll-off. This fact adds inherent ripple due to the estimation on the output estimated electrical position. This effect can be suppressed completely using frequency-based averaging of the resultant signal.

One advantage is that the stator fundamental current frequency is very well known because of the speed control and this frequency can be separated from the negative high-frequency current with a simple frequency averaged filter. This causes an additional delay to the position modulated negative rotating frame HF currents, but this delay is precisely known as a result of the knowledge of stator fundamental and can be compensated.

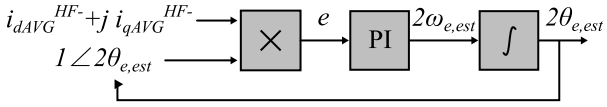

FIGURE 6. Built-in phase-locked loop control for position and speed estimation.

To this end, a simple variable length N-sample average filter as in (16) is used which consists of a simple sum and a division. N depends on the fundamental frequency of the stator currents and can be changed depending on the stator current frequency.

$$I_{dq,AVG}^{HF-} = \frac{1}{N}\sum_{1}^{N} I_{dq}^{HF-} \tag{16}$$

N can be varied to make torque producing stator currents have exactly zero influence on the position estimation. When the implementation simplicity and speed are considered, another approach is to use a bit shift divider corresponding to a fixed N. This speeds up the division with an acceptable error, depending on the injected frequency and operating speed. The injected frequency can be fine-tuned for simple division or increased further for better spectral separation. In the current case, N corresponds to 20 at the switchover frequency (300 rpm at 10 Hz with 10000 kHz sampling), which is the worst case.

The position information might be obtained directly from the remaining currents using an arctangent. However, the phase-locked loop (PLL) method provides a smoother estimation [13]. The PLL structure is a closed-loop estimator with a PI regulator for the position estimation as depicted in Fig. 6. The currents obtained in (16) and the estimated position from the output of the PLL is used to generate the position estimation error as shown in (17), which is essentially a vector cross product with a unity vector with angle $2\theta_{e,est}$. This error is fed to a PI regulator, then the output of the PI regulator is integrated once more to get the estimated position. This allows the intermediate variable between output of integrator and PI regulator to track the electrical frequency, which can be used for the speed estimation. The magnitude of (17) is irrelevant as regulating it to zero gives $\theta_{e,est} = \theta_e$.

$$e = \sqrt{\left(i_{dAVG}^{HF-}\right)^2 + \left(i_{qAVG}^{HF-}\right)^2}\, sin\left(2\left(\theta_e - \hat{\theta}_{e,est}\right)\right) \tag{17}$$

The complete system is given in Fig. 5. Since this is a speed control application, there is a PI regulator to regulate the speed, followed by the MTPA block described in (3) and (4). The current controllers used in the system are conventional PI regulators. The outer speed loop sampling frequency is 1 kHz while the inner current control loop sampling frequency is 10 kHz. The Inverter and SVPWM modulators are conventional two-level voltage source inverter and SVPWM modulator. Red blocks of Fig 5. show the proposed position and speed estimation system and the blue portions are the conventional PI based FOC. Another difference from the conventional control is the inclusion of current feedback filtering

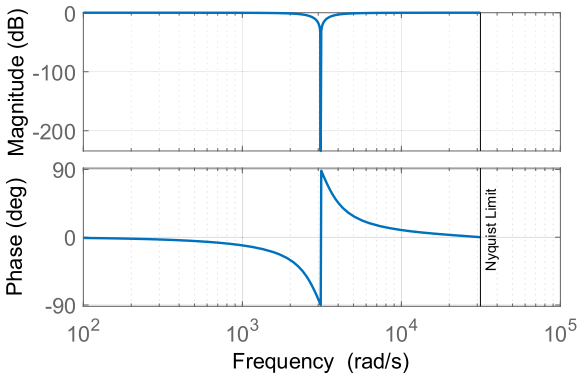

FIGURE 7. Bode plot of the current feedback notch filter.

which is implemented as a notch filter instead of a low-pass filter.

C. CURRENT FEEDBACK FILTERING

Another aspect of the conventional method that prevents high dynamic response of the current controllers is the feedback of the dq-axes currents. Whenever HF voltage is injected, induced HF currents are also picked up by the current controller feedback loops. This causes distortion on the current controller outputs. To mitigate this effect, filters are applied to the feedback loop of the current controllers to remove the high-frequency current components from the feedback loop.

For the proposed method, instead of low-pass filters, notch filters are used for improving the dynamic response in terms of the step response of current controllers. Since the current controllers have a large bandwidth, band-limited response of the low-pass filter causes current control degradation and overshoots, especially in the case of step changes in reference setpoints. Notch filter center frequency is the same with the injected high-frequency voltage. Fig. 7 gives the Bode plot of the used notch filter for a 10 kHz sample time. A fast step response is important in current feedback so as not to distort the controller current during step loads, hence the importance of very low phase lag outside of the band-stop region.

D. MAGNET POLARITY DETECTION

If the permanent magnet polarity is not determined correctly, the electrical position of the rotor is estimated with a 180° error resulting in an incorrect field orientation. To prevent this estimation error, permanent magnet polarity should be determined before closing the control loop [26]. The pilot voltage injection method is applied to predict the initial position of the rotor accurately. The logic of this method is based on comparing the q-axis current peak values by injecting two pilot voltages of different signs with the same amplitude and time intervals into the motor stator windings along the estimated q-axis as illustrated in Fig. 8 [27]. The applied pilot voltage vectors must be high and long enough to cause magnetic saturation [28]. The advantages of this technique are its simplicity, ease of application, and

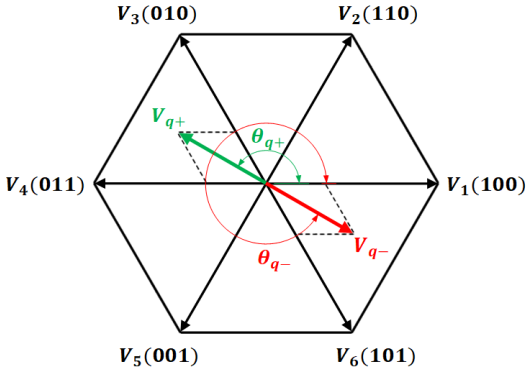

FIGURE 8. Pilot voltages in the three-phase inverter space vector plane.

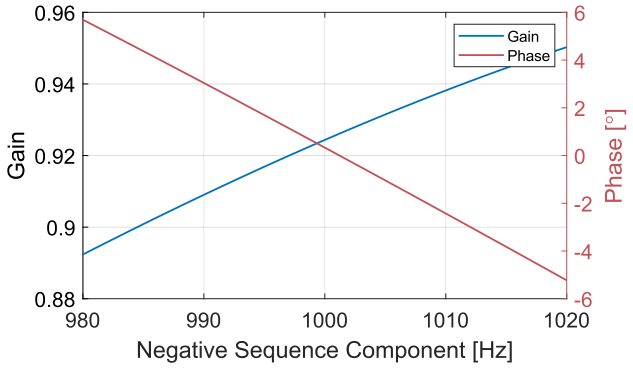

FIGURE 9. Band-pass filter gain and phase to negative rotating component.

shorter polarity detection time. During this step, the HFI process should be stopped and the current control should be disabled.

The current profile in two different directions will have different values as well as different rise times because of the magnetic saturation. The estimated initial position value is confirmed by checking the current magnitude after a few sampling times (or checking the amount of time in which direction the current rises above a pre-defined threshold). Slower rise time gives q-axis and if needed, estimated d-axis is adjusted accordingly. No significant torque is produced and the rotor does not move since the voltage is applied to the motor only in the q-axis direction.

E. POSITION ESTIMATION ERROR COMPENSATION

The total position estimation error is affected by numerous factors including but not limited to the current measurement shunts, their filter delays, sensor propagation delay, signal measuring, and processing delay. For the proposed method, the delay is mainly composed of N-sampled averaging and band-pass filtering. The band-pass estimation error given in (18) is obtained by calculating the phase shift created by the band-pass filter at the frequency difference between the rotor frequency and injected frequency.

$$2\Delta\hat{\theta}_{e_{comp}} = atan\left(\frac{\omega^2 - \omega_0^2}{\omega_g \omega}\right) \tag{18}$$

where;

$$\omega = 2(\omega_h - \omega_e) \tag{19}$$

The resultant delay is added to the estimated position, alongside N-sample averaging and current shunt filter phase delays. Signal propagation delay and sampling latency are omitted. Fig. 9 gives the gain and phase response to the negative sequence component of the resultant high-frequency currents. A first-order polynomial is fitted to the phase delay of the filter in different operating points of the motor for delay compensation in real time as a function of rotor speed. The gain correction is neglected.

F. SWITCHOVER AT LOW TO MEDIUM SPEED REGION

At the boundary of the HFSI and EEMF-sliding mode observer (SMO), a smooth switchover to medium – high-speed sensorless control is required. Simplified processing of the HFSI allows parallel operation of EEMF position estimation alongside HFSI position estimation, allowing a smooth switchover.

For the medium to high-speed region, the EEMF model of the PMaSynRM is used for position determination. The EEMF model and its components are given in (20) and (21) [29]. An SMO is used for driving the observer outputs which is based on (20) to (21). With the assumption of the d-axis steady state current, position information is extracted with a four-quadrant arctangent from alpha-beta components of the EEMF observer as in (22).

$$p\begin{bmatrix} i_\alpha \\ i_\beta \end{bmatrix} = \begin{bmatrix} \frac{-R_s}{L_q} & \frac{\omega_e(L_d - L_q)}{L_q} \\ \frac{-\omega_e(L_d - L_q)}{L_q} & \frac{-R_s}{L_q} \end{bmatrix} \begin{bmatrix} i_\alpha \\ i_\beta \end{bmatrix} + \frac{1}{L_q}\begin{bmatrix} u_\alpha \\ u_\beta \end{bmatrix} - \frac{1}{L_q}\begin{bmatrix} e_\alpha \\ e_\beta \end{bmatrix} \tag{20}$$

$$\begin{bmatrix} e_\alpha \\ e_\beta \end{bmatrix} = \left((L_d - L_q)\left(pi_d + \omega_e i_q\right) + \omega_e \lambda_{PM}\right)\begin{bmatrix} cos\,(\theta_e) \\ sin\,(\theta_e) \end{bmatrix} \tag{21}$$

$$\theta_{e,EEMF} = atan2\left(\frac{e_\beta}{e_\alpha}\right) \tag{22}$$

Additionally for the output filtering stage of the SMO, a variable band-pass frequency is used to account for operating speed change, enhancing position determination [29]. Finally, the speed is estimated with a filtered derivative from the estimated position information.

III. SIMULATION AND EXPERIMENTAL RESULTS

The PMaSynRM with ferrite magnets is used for the simulation and tests. The motor parameters are forementioned in Table 1. The sensorless control algorithm employs the HFI technique from zero speed up to 300 rpm and the EEMF-based position observer above 300 rpm which has good performance from medium to high speeds [29].

Thus, the system has ultimate estimation capability for full-range speed control. Since motor speed-dependent terms are neglected in the HFI technique, the method is prone to error as motor speed dependent terms become dominant with respect to injected frequency. Therefore, the HFI technique is utilized below the minimum speed at which the EEMF observer operation is not viable for this particular machine.

The sensorless speed control of the PMaSynRM with the HFI method is simulated in the MATLAB/Simulink environment using a 10 kHz, two-level SVPWM inverter with conventional PI controllers. The speed control is performed with estimated speed and position values as feedback. Speed control is verified with extensive simulations under full load with the HFI method down to a minimum speed of 15 rpm, corresponding to 0.5% of the base frequency, i.e., 0.5 Hz electrical cycle for the PMaSynRM. Position detection is accurate from zero speed, however the speed control under the full-load is dominated by the dynamics of the speed controller and the coupled load dynamics. Step direction reversal and on-load step response are also investigated, alongside switchover to the EEMF observer for FOC in the testing phase.

In the experimental process, the controller and driver algorithms are implemented on a Texas Instruments MCU (TMS320F28035). The power stage consists of a two-level inverter with a switching frequency of 10 kHz and a DC link voltage of 350 V. The input power, voltages and currents of the system are measured with a power meter (HIOKI 3337P). Kistler 4503A is used as the torque sensor and a MAGTROL AHB5 hysteresis brake is used as the load.

A. SIMULATION RESULTS

Closed-loop speed control simulations of the system with estimated position and speed are carried out for 15 and 300 rpms under rated load. Lower speed limit originates from the lowest speed achievable with the test system under full load due to the ripple characteristics of the load. Upper limit is the switchover speed between the sensorless techniques. All the speed values in between are not given for the sake of brevity. The injected voltage magnitude and frequency are 28 V_{peak} and 500 Hz, respectively.

The error in the estimation position used for reference frame transformations causes a reduction in the motor efficiency due to mismatched MTPA trajectory. In the simulations carried out, it is observed that a 2 degrees electrical error corresponds to 0.04% reduction for 15 rpm and 0.56% reduction for 300 rpm in the motor efficiency solely on this case.

A successful closed-loop speed control in the simulation environment is achieved with acceptable ripples of rotor speed compared to the speed reference and load torque with utilizing estimated motor speed. The position estimation for the starting and ramp speed response for 15 rpm are given in Fig. 10 and 11, respectively. The electrical position estimation error is around 1 degree and is approximately the same during the acceleration and steady-state conditions

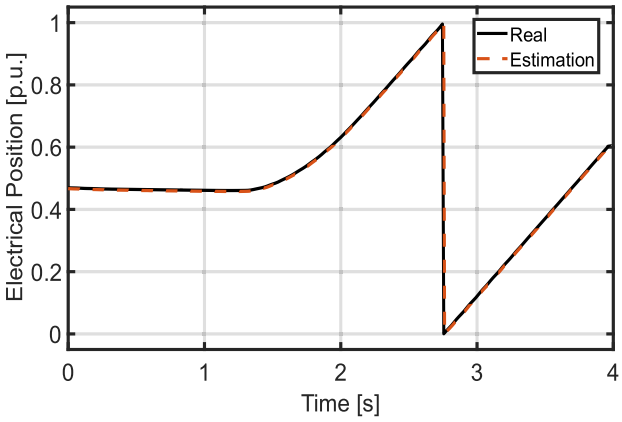

FIGURE 10. Simulated position estimation during starting transient under rated load 15 rpm.

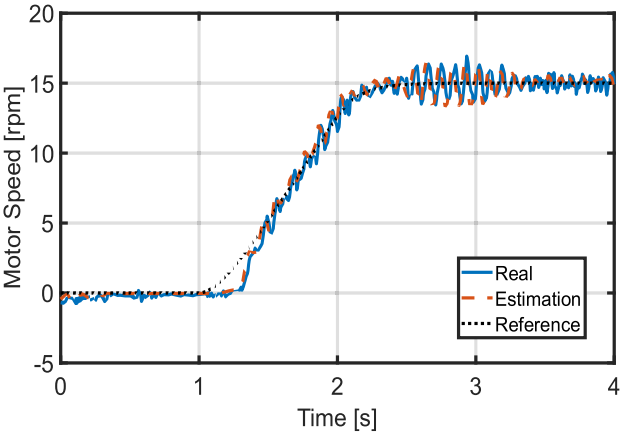

FIGURE 11. Simulated ramp speed reference tracking from zero speed to 15 rpm under 100% load.

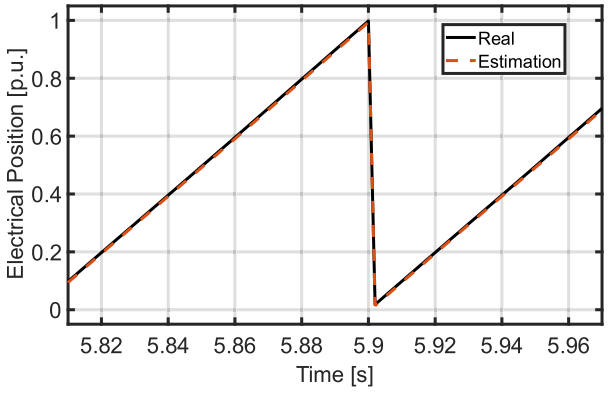

FIGURE 12. Simulated position estimation during steady-state under rated load 300 rpm.

under full load. The maximum ripple of the rotor speed at 15 rpm is about 23%. Further decrease in the ripple percentage is possible by tuning or changing the speed controller structure.

The same speed reference profile is applied up to 300 rpm which is the switchover speed. The position estimation and

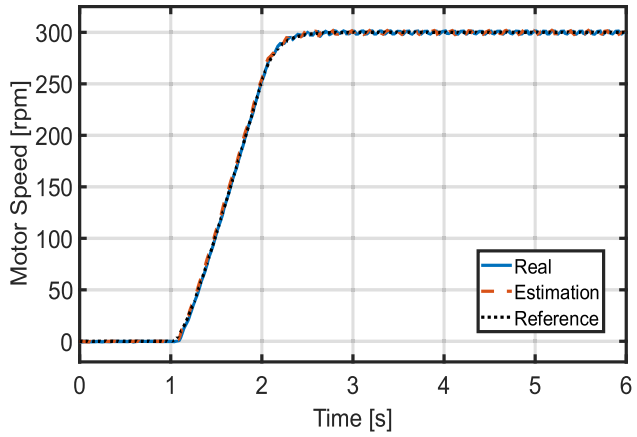

FIGURE 13. Simulated ramp speed reference tracking from zero speed to 300 rpm under 100% load.

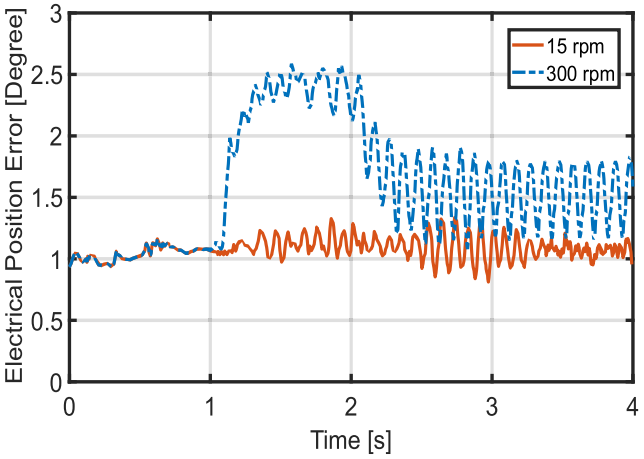

FIGURE 14. Simulated rotor electrical position estimation errors at 15 and 300 rpm.

speed reference tracking are given in Fig. 12 and 13 for respectively. At steady-state, the maximum speed ripple is 1.67% according to the reference speed. Besides, there is an increase in the position estimation error with higher motor speed as expected.

The total position estimation error over time is given in Fig. 14 for 15 and 300 rpms. Degradation in the position estimation during speed transient is evident. This is due to the dynamic response of the whole system, including the filter transients (mainly the aforementioned deviation from filter center frequency) and averaging delays. In steady state, the average position estimation error is less than 2 degrees electrical at 300 rpm and around 1 degree electrical at 15 rpm. The steady-state errors are in between 1 and 2 degrees electrical in these speed range.

B. TEST RESULTS

The tests are carried out from zero speed to 300 rpm under no-load, rated load and rated current. Correct position and field orientation are achieved in the given speed range. The injected voltage is as low as 11.4 V_{rms} at 500 Hz for the

TABLE 2. HF injection test values and filter parameters.

Parameter	Value
Injected Voltage Magnitude	11.4 V
Resulting avg. HF Current Amplitude	85 mA
Injected Voltage Frequency	500 Hz
Band-pass filter passband width	330 Hz
Band-stop filter stopband width	400 Hz

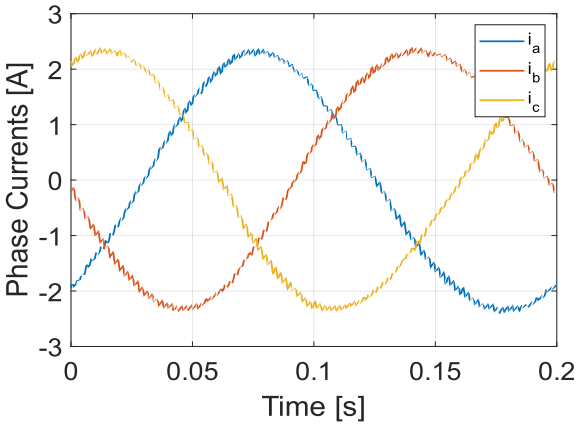

FIGURE 15. Phase currents with HF currents impressed at 100% load 150 rpm – test data.

accurate position determination. The voltage value is gradually decreased during the tests starting from 35 V_{rms} to reach the lowest value that allows unhindered operation. 11.4 V_{rms} injected voltage results in currents as high as 105 mA_{peak}, depending on the rotor position. The average value of this current is 85 mA_{peak} for each phase around the whole revolution. Band-pass filter band width is 330 Hz. Stopband of notch filter used for current feedback is 400 Hz. Table 2 gives an overview of the HF injection test values and filter parameters.

Resultant three-phase currents with fundamental and high-frequency components at 100% load and 150 rpm are presented in Fig. 15. The currents are transformed into positive high-frequency frame and band-pass filtered. The filter outputs are then transformed into negative high-frequency frame and moving averaged to remove the effects of stator current component explained in the preceding chapters. Fig. 17 gives the negative rotating d-q components of the high-frequency currents and their N-sample averaged versions. The frequency of these signals is modulated with the double frequency of rotor electrical position, as it is evident from the graph. The rotating speed is 300 rpm, with closed-loop control. The test bed is shown in Fig. 16.

N-sample averaging provides smoothing of the position information carrying currents by filtering out stator fundamental current frequency. As shown in Fig. 17, a fair amount of fundamental stator current is passing through the band-pass filter. A huge amount of current distortion is present combined with the transformed negative high-frequency

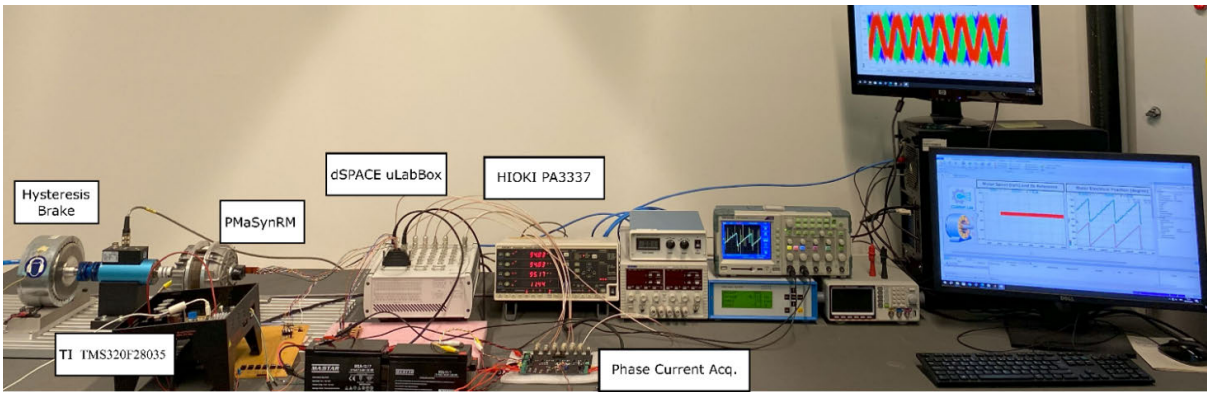

FIGURE 16. Experimental setup.

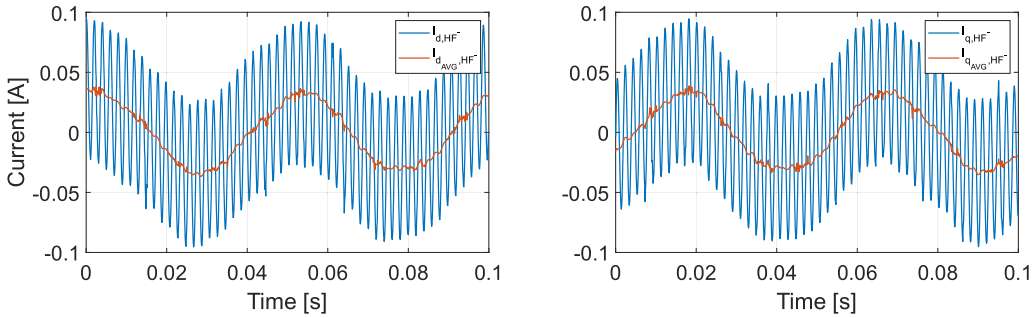

FIGURE 17. N-sample averaged filtered high-frequency negative frame d&q current components with unfiltered counterparts.

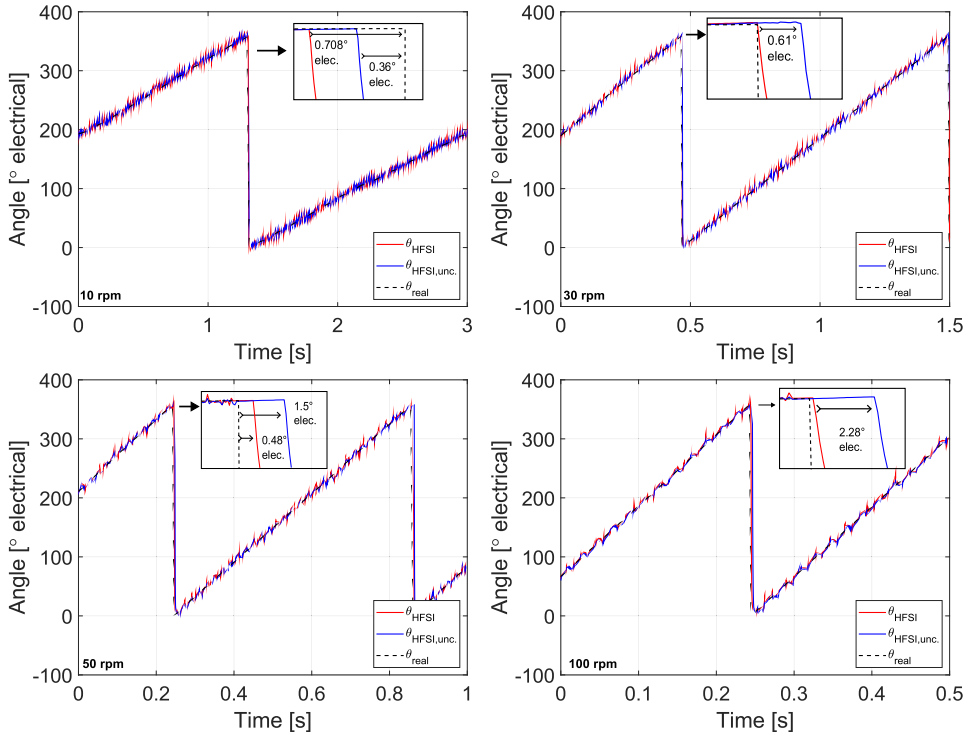

FIGURE 18. Estimation values of rotor position at 10 (0.33 Hz), 30 (1 Hz), 50 (1.6 Hz) and 100 (3.66 Hz) rpm.

current (amplitude around 40 mA). It is evident from (12) that this current is localized at the frequency $(\omega_{hf} + \omega_e)$. A frequency-based N-sample averaging at this specific frequency nearly removes this frequency component with a

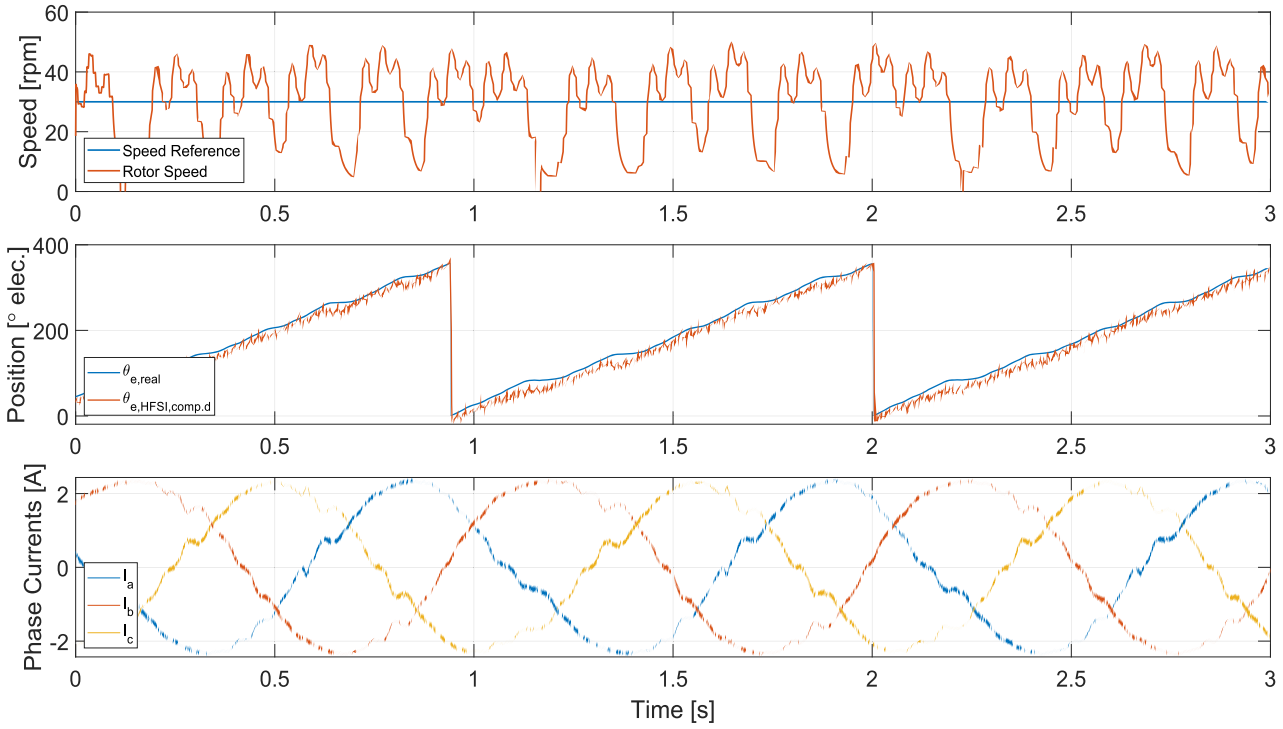

FIGURE 19. HFSI closed loop under 1 Nm average torque with 30% disturbance torque ripple at load at 30 rpm.

lower delay and system complexity compared to an additional synchronous frame filtering. Averaged currents of Fig. 17 are used for the position determination in PLL.

Initially, no-load conditions are analyzed experimentally. To give a comparison estimated position without any compensation is given alongside compensated one in the figures. The speed loop is closed with HFSI position estimation with the no-load. No load conditions correspond to the hysteresis brake inertia and combined Coulomb and viscous friction torque of the load and motor. Fig. 18 presents the position estimation performance compared to the actual position with and without compensation for the speeds of 15, 50, 100 and 300 rpm. The proposed method provides a very high accuracy in position estimation with errors up to 0.708 degree electrical. Compared to the literature this is an improvement. Reference [13] shows a maximum position error of 0.606 at 75 rpm with a 1.6 kW PMSM while [14] shows a 0.573 degree error under no-load at 300 rpm and 11.459 degree under 0.14 pu load at 200 rpm. Also under 200% overload, [15] shows 1.318 degree error at 400 rpm for a 1 kW PMSM. For the HFPVI injection on the other hand, different studies with different motors show 4.011, 5.73 and 7.779 degree position errors for 15, 300 and 600 rpm respectively under no-load [10]. Other studies also show the position errors of HFPVI for the loaded cases as 5.157, 5 and 7 degrees for 300, 100 and 200 rpm, respectively [11], [12].

The load is usually highly inertial for washing machine applications and it is influenced by the contents of the washer

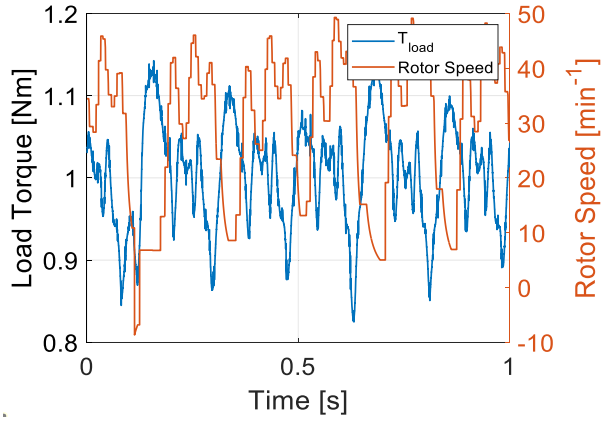

FIGURE 20. Torque and speed profile over time under 85% load at 30 rpm.

drum. Additional periodic torque distortions are present during the washing cycle because of the rolling clothes inside the drum. This load case is realized in the test bench with a hysteresis brake. The slotting effect of the hysteresis brake creates an effective torque ripple as a disturbance over an average load torque value. For this operating condition, speed regulation and position estimation are given in Fig 19.

Position error is fixed as 1 degree electrical that is the same as in the simulations. Fig. 19 also shows the phase currents. The distortion caused by the speed fluctuation is obvious

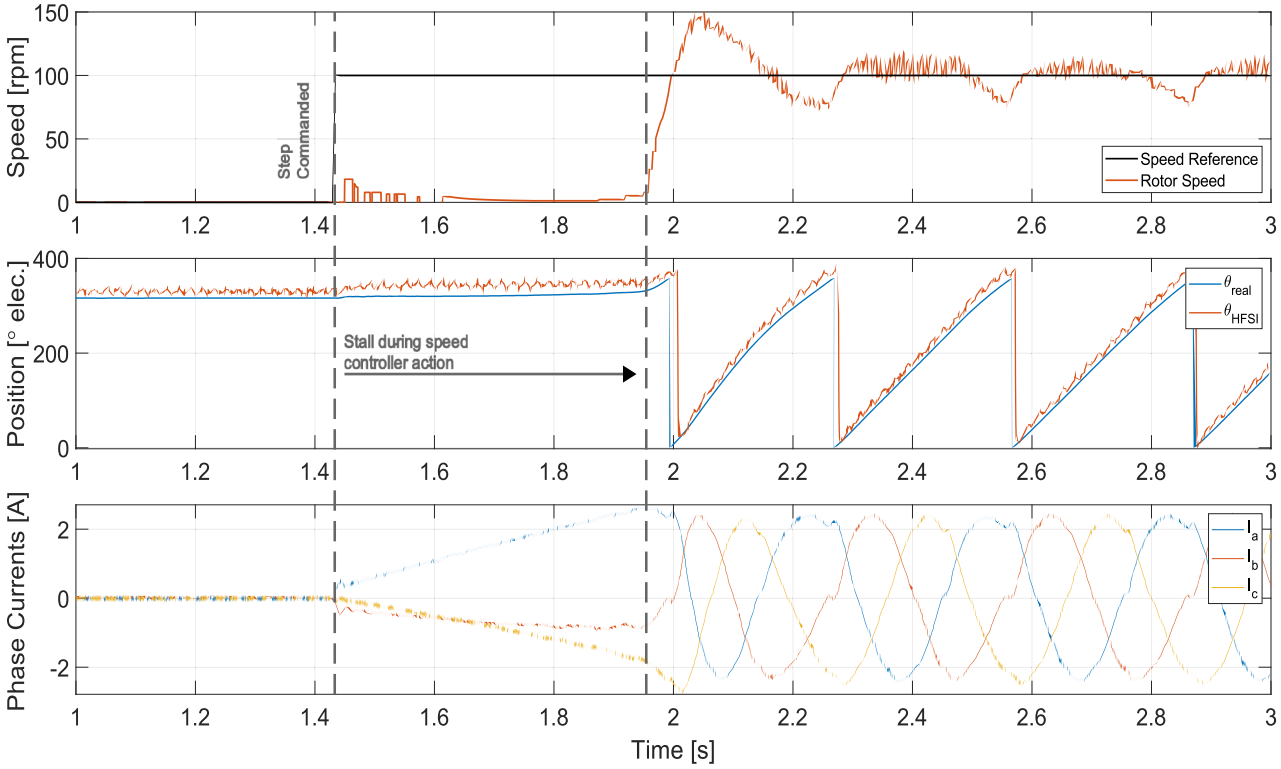

FIGURE 21. Step response to 100 rpm reference under full load without stall torque.

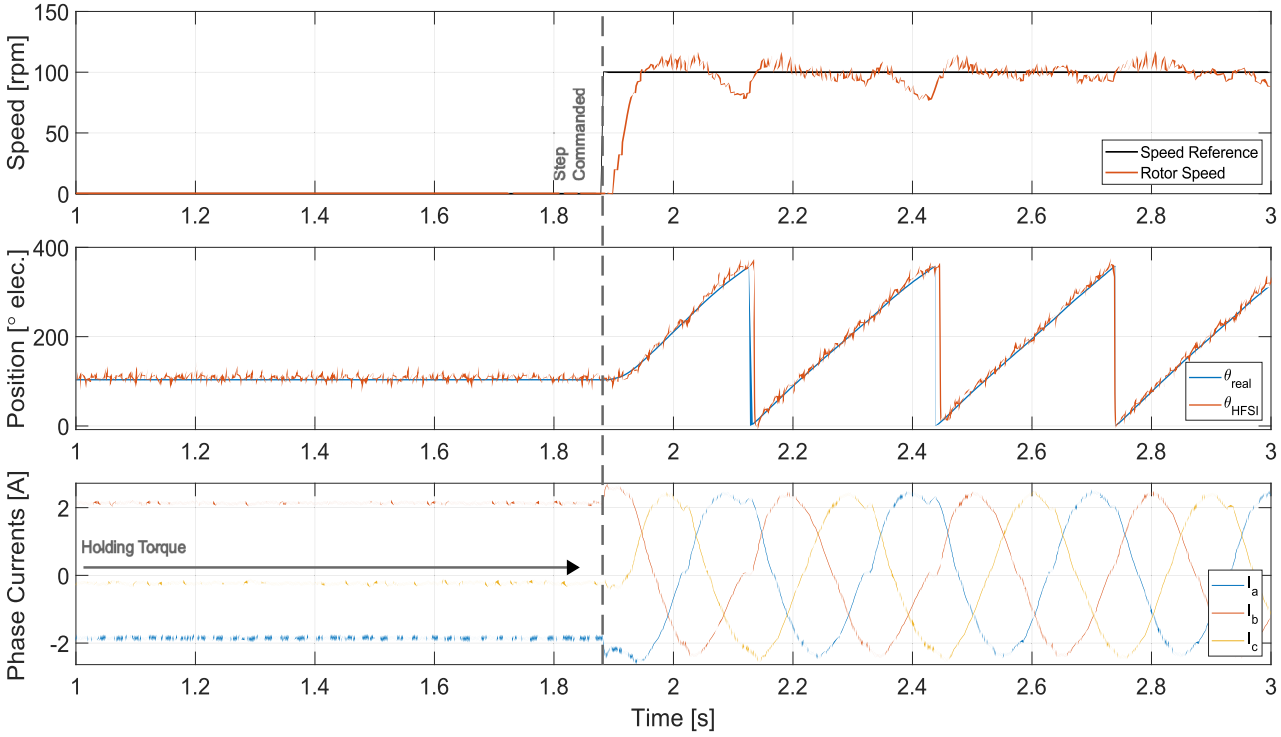

FIGURE 22. Step response to 100 rpm reference under full load with stall torque (hold condition).

in the phase currents. Thus, extra fine-tuning of the speed controller is often needed at very low speeds or switching to position control instead of speed control would be more beneficial.

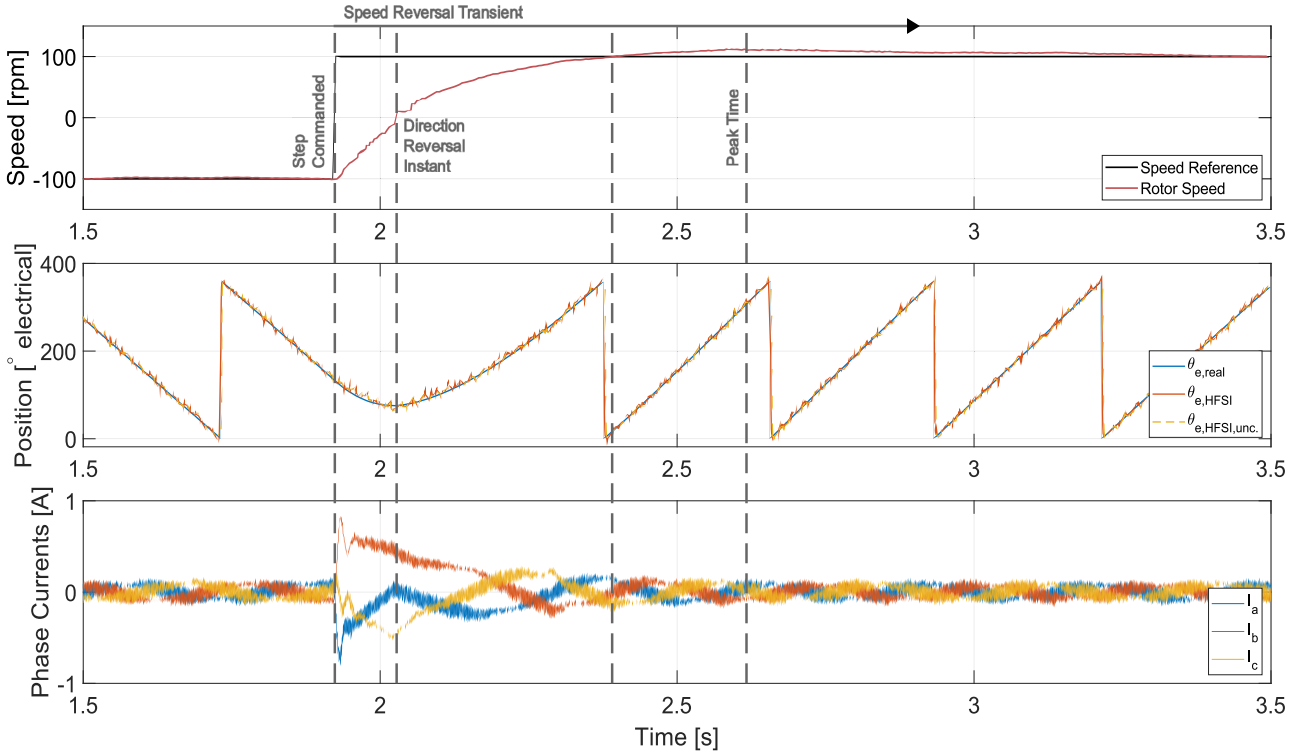

FIGURE 23. Speed reversal from -100 rpm to 100 rpm in step manner.

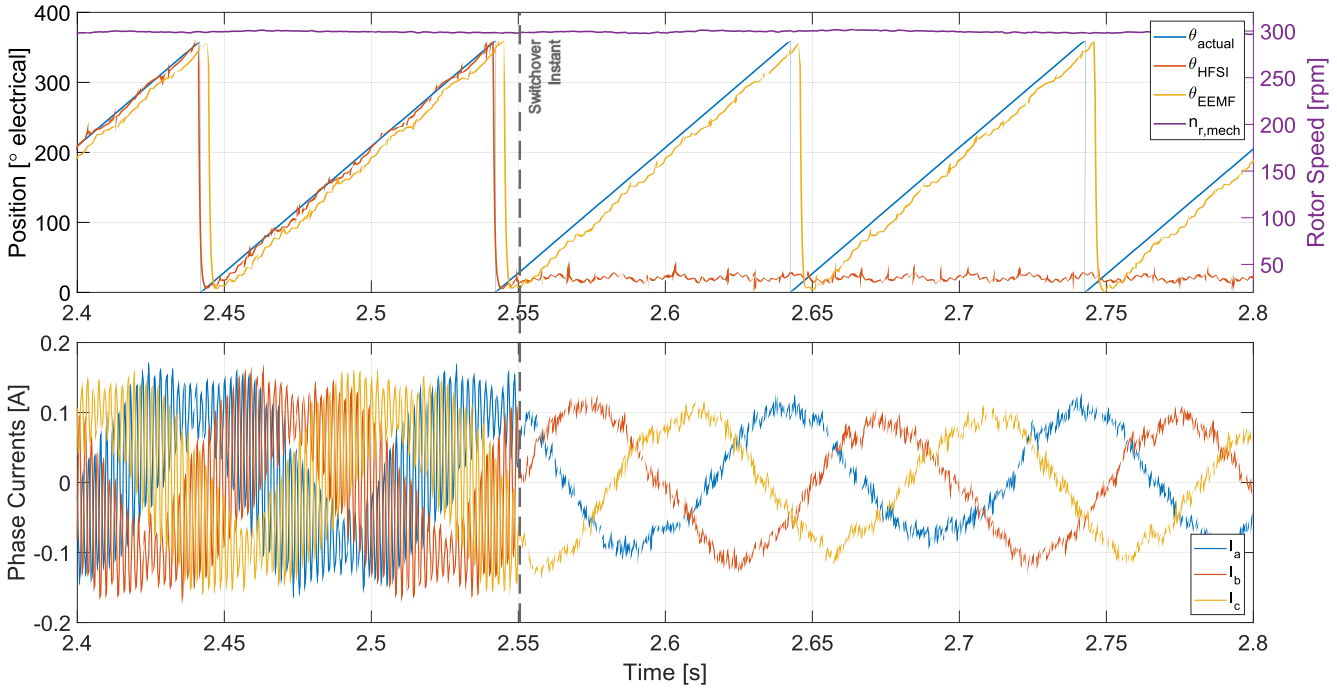

FIGURE 24. Speed and current transients of switchover from HFSI to EEMF position observer at no load – experimental results.

This is apparent at the load torque and speed profile given in Fig. 20 for 30 rpm where the FOC speed control loop is closed with the HFSI position and speed feedback. Load torque ripple is approximately 30% peak-to-peak, with 1 Nm

average. Speed is 30 rpm, 1 Hz electrical (1% of base) under 85% load.

In addition to the load tests, step speed command tests under full load from zero speed are carried out to further demonstrate the robustness of the proposed method. The step speed response under load is crucial because of the representation of the worst case in terms of both speed and current transients. Under step transients, it is vital for the PLL not to lose sync with the rotor position. If the rotor position is not tracked well enough, either PLL is slow to respond to the error coming from position modulated negative frame components, or band-pass filtering and N-sample averaging is allowing too much spectral component of the stator fundamental current to pass.

Full load step response tests are carried out in two different cases; under zero stall torque and under 0.83 p.u. stall torque. A speed reference of 100 rpm from zero speed is commanded under full load and 1.2 Nm and step response are analyzed. Fig. 21 shows the speed step response with the phase currents and position estimation under zero stall torque and Fig. 22 gives the step response under 1 Nm stall torque, up to 1.2 Nm full load. The rotor speed reaches to commanded reference speed in about a second including the delay of the speed controller. Fig. 21 and 22 also present the position tracking under speed and current transients.

Maximum position estimation error is approximately 2 degrees electrical under load including the filter compensation. The injected voltage value is not changed during transients and steady state. The position error increases during speed transients and reference tracking because of the compensation which is a function of the estimated speed from the PLL. The estimated speed from the PLL is filtered by a 5 Hz low-pass filter, hence there is a delay to speed response. Since the filter delay compensation value is tied to the estimated speed, compensation delay is also present.

The HFSI position estimation performance is also tested for speed reversals. The speed reversal in a step manner is investigated for the unloaded case. A good step speed reversal is achieved with the proposed method without any significant position determination error increase. The speed response, position estimation error and phase currents from -100 rpm to $+100$ rpm are given in Fig. 23. Other speed values are left out as the only difference is the amount of overshoot, settling time and transient current magnitude.

The standstill starting operation with step reference under closed loop HFSI control and rated load is scarce in the literature as it is an extreme case. The proposed method includes the applicability of step commands for the HFSI sensorless control technique. Conventional methods of HFRVI and HFPVI use between 16.8% to 55.6% of the rated voltage as the injected voltage magnitude [16], [24], [30]. With the proposed method, the injection of 8.7% of the rated phase voltage (down to 5% of DC-link) is a promising value even though, most of the voltage is already available at low speeds.

Lastly, the switch from low-speed estimation to medium-to-high speeds estimation transients are presented in Fig. 24 under no load. The method used for medium speeds is the EEMF model combined with an SMO. After the switchover is done, the injected voltage is removed and the position feedback switches to the SMO output. There is no noticeable transient in the rotor speed. Both algorithms are able to work from zero speed up to the switchover speed, where the HFSI is cancelled after the switch. This shows the pertinence of two different methods simultaneously to cover the whole speed range using a low-cost MCU.

IV. CONCLUSION

This paper presents a lean approach to sensorless position determination of PMaSynRMs with conventional rotating high-frequency voltage injection. The following points summarize the proposed method's advantages:

- Correct position estimation with injected voltage magnitudes of 5% of the DC-link voltage with maximum error of 0.708 degree electrical.
- Reduction in the total number of filtering stages from two to one and total coordinate transformations by half, meaning less need for filter fine-tuning and delay and gain compensation, simplifying the overall design stage.
- Reduced complexity of the whole system for easier implementation
- Reducing development time by removing the current controller bandwidth constraints, allowing the same current controller to be used in zero-low and medium-high speed regions.
- Operation with current feedback filtering and parallel operation of an SMO based Back-EMF observer result in 47% CPU overhead (without optimizations), allowing additional functionality.

In addition, the proposed approach is very robust against high transient operation, full load at very low speeds down to 1% of base frequency, where performance can be further enhanced with other controllers than PI. The step speed response is also demonstrated, without any deterioration to the estimated position due to the influence of current and speed gradients.

A good speed reversal at very low speeds (from -1% of the rated to $+1\%$) is also achieved, proving proposed methods ability to handle high transient currents and speeds. Applicability is also shown to be run on a low-cost MCU alongside another sensorless position estimation algorithm such as an SMO owing to the proposed method's lightweight computational burden. These features make the proposed solution a good candidate for home appliance applications where the cost is a major factor and system complexity reduction in both software and hardware is crucial. The proposed method can be further improved in future work by considering its applicability to other motor types, especially those with lower saliency ratios compared to PMaSynRM. The robustness, response time, accuracy and settling time of the position and

velocity estimator and the position error compensator can be further investigated under high disturbance load torques.

REFERENCES

[1] A. Oprea and D. Floricau, "Efficient topology of powering a washing machine using a permanent magnet synchronous motor," in *Proc. Int. Conf. Appl. Theor. Electr. (ICATE)*, Craiova, Romania, May 2021, pp. 1–4.

[2] G. Wang, M. Valla, and J. Solsona, "Position sensorless permanent magnet synchronous machine drives—A review," *IEEE Trans. Ind. Electron.*, vol. 67, no. 7, pp. 5830–5842, Jul. 2020.

[3] L. A. S. Ribeiro, M. W. Degner, F. Briz, and R. D. Lorenz, "Comparison of carrier signal voltage and current injection for the estimation of flux angle or rotor position," in *Proc. Conf. Rec. IEEE Ind. Appl. Conf. Thirty-Third IAS Annu. Meeting*. Louis, MO, USA: IEEE, 1998, pp. 452–459.

[4] X. Dianguo, J. Xinhai, and C. Wei, "Sensorless control of synchronous reluctance motors," in *Proc. IEEE Transp. Electrific. Conf. Expo, Asia–Pacific (ITEC Asia–Pacific)*, Harbin, Aug. 2017, pp. 1–4.

[5] Z. Zhang and J. Lamb, "High frequency injection transient disturbance mitigation for sensorless control of salient pole machines," in *Proc. IEEE Energy Convers. Congr. Exposit. (ECCE)*, Vancouver, BC, Canada, Oct. 2021, pp. 4748–4753.

[6] Y. Li, H. Hu, and P. Shi, "A review of position sensorless compound control for PMSM drives," *World Electric Vehicle J.*, vol. 14, no. 2, p. 34, Jan. 2023.

[7] L. Gou, C. Wang, X. You, M. Zhou, and S. Dong, "IPMSM sensorless control for zero- and low-speed regions under low switching frequency condition based on fundamental model," *IEEE Trans. Transport. Electrific.*, vol. 8, no. 1, pp. 1182–1193, Mar. 2022.

[8] A. Messali, M. A. Hamida, M. Ghanes, and M. Koteich, "Estimation procedure based on less filtering and robust tracking for a self-sensing control of IPMSM," *IEEE Trans. Ind. Electron.*, vol. 68, no. 4, pp. 2865–2875, Apr. 2021.

[9] H. W. De Kock, M. J. Kamper, and R. M. Kennel, "Anisotropy comparison of reluctance and PM synchronous machines for position sensorless control using HF carrier injection," *IEEE Trans. Power Electron.*, vol. 24, no. 8, pp. 1905–1913, Aug. 2009.

[10] Y. Zhang, Z. Yin, C. Du, Y. Wang, and X. Sun, "An enhanced high frequency pulsating voltage injection method based on immune algorithm for sensorless IPMSM drives," in *Proc. Int. Power Electron. Conf. (IPEC-Niigata -ECCE Asia)*, Niigata, Japan, May 2018, pp. 2204–2209.

[11] L. Ortombina, D. Pasqualotto, F. Tinazzi, and M. Zigliotto, "Comprehensive analysis and design of a pulsating signal injection-based position observer for sensorless synchronous motor drives," *IEEE J. Emerg. Sel. Topics Power Electron.*, vol. 10, no. 2, pp. 1925–1934, Apr. 2022.

[12] J. Hu and B. Tian, "Sensorless control of PMSM based on a high-frequency injection using a complex-valued filter," in *Proc. IEEE 6th Int. Electr. Energy Conf. (CIEEC)*, Hefei, China, May 2023, pp. 442–447.

[13] A. Malekipour, A. Corne, L. Garbuio, P. Granjon, and L. Gerbaud, "A closed-loop PMSM sensorless control based on the machine acoustic noise," *IEEE Trans. Ind. Electron.*, vol. 70, no. 10, pp. 9859–9869, Oct. 2023.

[14] X. Sun, F. Cai, Z. Yang, and X. Tian, "Finite position control of interior permanent magnet synchronous motors at low speed," *IEEE Trans. Power Electron.*, vol. 37, no. 7, pp. 7729–7738, Jul. 2022.

[15] L. Ortombina, M. Berto, and L. Alberti, "Sensorless drive for salient synchronous motors based on direct fitting of elliptical-shape high-frequency currents," *IEEE Trans. Ind. Electron.*, vol. 70, no. 4, pp. 3394–3403, Apr. 2023.

[16] J.-H. Jang, S.-K. Sul, J.-I. Ha, K. Ide, and M. Sawamura, "Sensorless drive of surface-mounted permanent-magnet motor by high-frequency signal injection based on magnetic saliency," *IEEE Trans. Ind. Appl.*, vol. 39, no. 4, pp. 1031–1039, Jul. 2003.

[17] D. Raca, P. Garcia, D. D. Reigosa, F. Briz, and R. D. Lorenz, "Carrier-signal selection for sensorless control of PM synchronous machines at zero and very low speeds," *IEEE Trans. Ind. Appl.*, vol. 46, no. 1, pp. 167–178, Jan. 2010.

[18] W. Qian, X. Zhang, F. Jin, H. Bai, D. Lu, and B. Cheng, "Using high-control-bandwidth FPGA and SiC inverters to enhance high-frequency injection sensorless control in interior permanent magnet synchronous machine," *IEEE Access*, vol. 6, pp. 42454–42466, 2018.

[19] Z. Yang, K. Wang, and X. Sun, "Novel random square-wave voltage injection method based on Markov chain for IPMSM sensorless control," *IEEE Trans. Power Electron.*, vol. 37, no. 11, pp. 13147–13157, Nov. 2022.

[20] J. Chen, Y. Fan, W. Wang, C. H. T. Lee, and Y. Wang, "Sensorless control for SynRM drives using a pseudo-random high-frequency triangular-wave current signal injection scheme," *IEEE Trans. Power Electron.*, vol. 37, no. 6, pp. 7122–7131, Jun. 2022.

[21] W. T. Villet, M. J. Kamper, P. Landsmann, and R. Kennel, "Evaluation of a simplified high frequency injection position sensorless control method for reluctance synchronous machine drives," in *Proc. 6th IET Int. Conf. Power Electron., Mach. Drives (PEMD)*, Jan. 2012, pp. 62–61.

[22] S. Wang, K. Yang, and K. Chen, "An improved position-sensorless control method at low speed for PMSM based on high-frequency signal injection into a rotating reference frame," *IEEE Access*, vol. 7, pp. 86510–86521, 2019.

[23] Z. Wang, B. Yao, L. Guo, X. Jin, X. Li, and H. Wang, "Initial rotor position detection for permanent magnet synchronous motor based on high-frequency voltage injection without filter," *World Electric Vehicle J.*, vol. 11, no. 4, p. 71, Nov. 2020.

[24] G. Xie, K. Lu, S. K. Dwivedi, J. R. Rosholm, and F. Blaabjerg, "Minimum-voltage vector injection method for sensorless control of PMSM for low-speed operations," *IEEE Trans. Power Electron.*, vol. 31, no. 2, pp. 1785–1794, Feb. 2016.

[25] K. Akgul, A. Tap, A. F. Ergenc, M. Yilmaz, and L. T. Ergene, "Sensorless control of PMaSynRM with HFI method using modified PLL for low speeds," in *Proc. Int. Conf. Electr. Mach. (ICEM)*, Sep. 2022, pp. 1457–1463.

[26] Z. Wang, Z. Cao, and Z. He, "Improved fast method of initial rotor position estimation for interior permanent magnet synchronous motor by symmetric pulse voltage injection," *IEEE Access*, vol. 8, pp. 59998–60007, 2020.

[27] E. Trancho, E. Ibarra, A. Arias, I. Kortabarria, and P. Prieto, "A practical approach to HFI based sensorless control of PM-assisted synchronous reluctance machines applied to EVs and HEVs," in *Proc. IECON 43rd Annu. Conf. IEEE Ind. Electron. Soc.*, Oct. 2017, pp. 1735–1740.

[28] S.-C. Yang, S.-M. Yang, and J.-H. Hu, "Robust initial position estimation of permanent magnet machine with low saliency ratio," *IEEE Access*, vol. 5, pp. 2685–2695, 2017.

[29] A. Tap, K. Akgul, A. F. Ergenc, M. Yilmaz, and L. T. Ergene, "A comparison of sensorless MTPA and quasi-MPF control for VSD-PMaSynRM," in *Proc. IECON 47th Annu. Conf. IEEE Ind. Electron. Soc.* Toronto, ON, Canada: IEEE, Oct. 2021, pp. 1–6.

[30] H. Zhu, X. Xiao, and Y. Li, "A simplified high frequency injection method for PMSM sensorless control," in *Proc. IEEE 6th Int. Power Electron. Motion Control Conf.*, May 2009, pp. 401–405.

A. TAP received the B.Sc. and M.Sc. degrees in electrical engineering from Istanbul Technical University, in 2015 and 2017, respectively, where he is currently pursuing the Ph.D. degree in electrical engineering. He is an E-Drive Systems Engineer with AVL Research and Engineering Turkey. His research interest includes the design and control of permanent magnet synchronous machines and drives.

K. AKGUL received the B.Sc. degree in electrical engineering and control and automation engineering and the M.Sc. degree in electrical engineering from Istanbul Technical University (ITU), Istanbul, Turkey, in 2020 and 2023, respectively. In 2020, he joined the Computational Electromechanical Systems Research Group (CEMSys), ITU, where he is currently a Research Assistant. His current research interests include alternative control techniques and sensorless control of new-generation electrical machines.

A. F. ERGENC received the B.Sc. and M.Sc. degrees in control and computer engineering from Istanbul Technical University (ITU), Istanbul, Turkey, in 1999 and 2001, respectively, and the Ph.D. degree in mechanical engineering from the University of Connecticut, Storrs, CT, USA, in 2007. He is currently an Associate Professor with the Department of Control and Automation Engineering, ITU. His research interests include time-delayed systems, motion control systems, mechatronics, industrial automation, and instrumentation.

M. YILMAZ (Senior Member, IEEE) received the B.Sc., M.Sc., and Ph.D. degrees from the Department of Electrical Engineering, Istanbul Technical University (ITU), Istanbul, Turkey, in 1995, 1999, and 2005, respectively. He was a Postdoctoral Researcher with the University of Illinois at Urbana–Champaign (UIUC), from 2007 to 2008, and a Visiting Scholar, from 2011 to 2012. He is currently an Associate Professor with ITU. His research interests include power electronics and electrical machine design, control, optimization, and reliability modeling in motor drives and electric drive vehicles, including electric, hybrid, and plug-in electric vehicles.

L. T. ERGENE (Senior Member, IEEE) received the B.Sc. and M.Sc. degrees in electrical engineering from Istanbul Technical University (ITU), in 1992 and 1995, respectively, and the Ph.D. degree in electric power engineering from the Rensselaer Polytechnic Institute (RPI), Troy, NY, USA, in 2003. During the Ph.D. degree, she was a Support and Consulting Engineer with Magsoft Corporation, Clifton Park, NY, USA, from 1999 to 2003. Following one year of postdoctoral experience, in 2003, she gave lectures with RPI as an Adjunct Faculty Member, in 2004. She is currently a Full Professor of electrical engineering with ITU and a Coordinator with the Computational Electromechanical Systems (CEMSys) Research Group, ITU. Her research interests include design, modeling, and control of electrical machines, renewable energy, and numerical computation.